Available online at www.sciencedirect.com
ScienceDirect
Journal of the European Ceramic Society 30 (2010) 1707–1715
www.elsevier.com/locate/jeurceramsoc

Luminescent properties of rare earth (Er, Yb) doped yttrium aluminium garnet thin films and bulk samples synthesised by an aqueous sol–gel technique

Edita Garskaite [a], Mikael Lindgren [b], Mari-Ann Einarsrud [a], Tor Grande [a,*]

[a] *Department of Materials Science and Engineering, Norwegian University of Science and Technology, 7491 Trondheim, Norway*
[b] *Department of Physics, Norwegian University of Science and Technology, 7491 Trondheim, Norway*

Received 22 June 2009; received in revised form 2 December 2009; accepted 4 January 2010
Available online 25 January 2010

Abstract

Yttrium aluminium garnet (YAG) powders and thin films deposited on silicon substrates were prepared by an aqueous sol–gel route using metal nitrates. The sol–gel process resulted in an amorphous gel, and the thermal decomposition and successive crystallization were characterized by thermal analysis and X-ray diffraction. Powders were prepared by heat treatment of the amorphous gel, while crack-free thin films of densely packed nano-crystalline particles were obtained on silicon substrates by dip-coating technique. Photoluminescence (PL) properties as well as up-conversion (anti-stoke emission) of Er, Yb co-doped YAG phosphors were investigated. Green (555 nm) and red (650 nm) photoluminescence up-conversion emissions arising due to $^4S_{3/2} \rightarrow {}^4I_{15/2}$ and $^4F_{9/2} \rightarrow {}^4I_{15/2}$ transitions, respectively for Er^{3+} ion were observed. Photoluminescence and radiative life-times of the exited states of Er^{3+} in the visible and near IR ranges are also reported.

Keywords: YAG; Sol–gel process; Films; Optical properties

1. Introduction

Yttrium aluminium garnet (YAG, $Y_3Al_5O_{12}$) ceramics are used in numerous applications as structural and engineering materials and as host for solid state lasers and phosphors.[1–9] YAG demonstrates a high chemical stability, low electrical conductivity as well as high resistance to creep.[6,7,10–12] Moreover, YAG is doped with trivalent erbium (Er^{3+}) and ytterbium (Yb^{3+}) emits light in UV, visible and IR spectrum. Also, Er^{3+} and Yb^{3+} can convert photons from the infrared (IR) to the visible light by multiphoton absorption processes, which could be attractive for the light harvesting applications. The photoluminescence (PL) properties of phosphors strongly depend on the host lattice, type and concentration of activator ion,[13] crystallite and particle size, and surface morphology.[14]

The conventional route to YAG is the solid state synthesis method, but in order to achieve a large degree of homogeneity, small particle size and thin film soft chemistry techniques are desired. YAG and rare earth doped YAG thin films and powders have been produced by various techniques, such as electrochemical synthesis,[15] spray-inductively coupled plasma,[16] plasma spray process,[17] pulsed laser deposition (PLD),[18] sol–gel[19–21] and metal-organic chemical vapour deposition (MOCVD).[22] In order to achieve desirable properties of the thin films, precise control of phase homogeneity, particle size and morphology is necessary. Thus, the synthesis method is important for controlling the properties, the cost and possible applications of the films.[4,6,16,21,22] Wu et al. reported film synthesis by the sol–gel method using acetate and alkoxide precursors.[20,21] Jia et al. reported synthesis of thin films by Pechini sol–gel dip-coating method using citric acid and polyethylene glycol (PEG) as chelating and cross-linking agents, respectively.[23]

Lanthanide ions with luminescent properties are readily incorporated in host materials as the f-electrons constituting the photoactive center is well shielded.[24–26] However, in order to control parasitic quenching mechanisms as well as introducing more sophisticated photo-activity, some kind of organic cage or complex is needed, as shown e.g., for dendrimers,[27–29]

* Corresponding author. Tel.: +47 735 94084; fax: +47 735 91105.
E-mail address: tor.grande@material.ntnu.no (T. Grande).

0955-2219/$ – see front matter © 2010 Elsevier Ltd. All rights reserved.
doi:10.1016/j.jeurceramsoc.2010.01.001

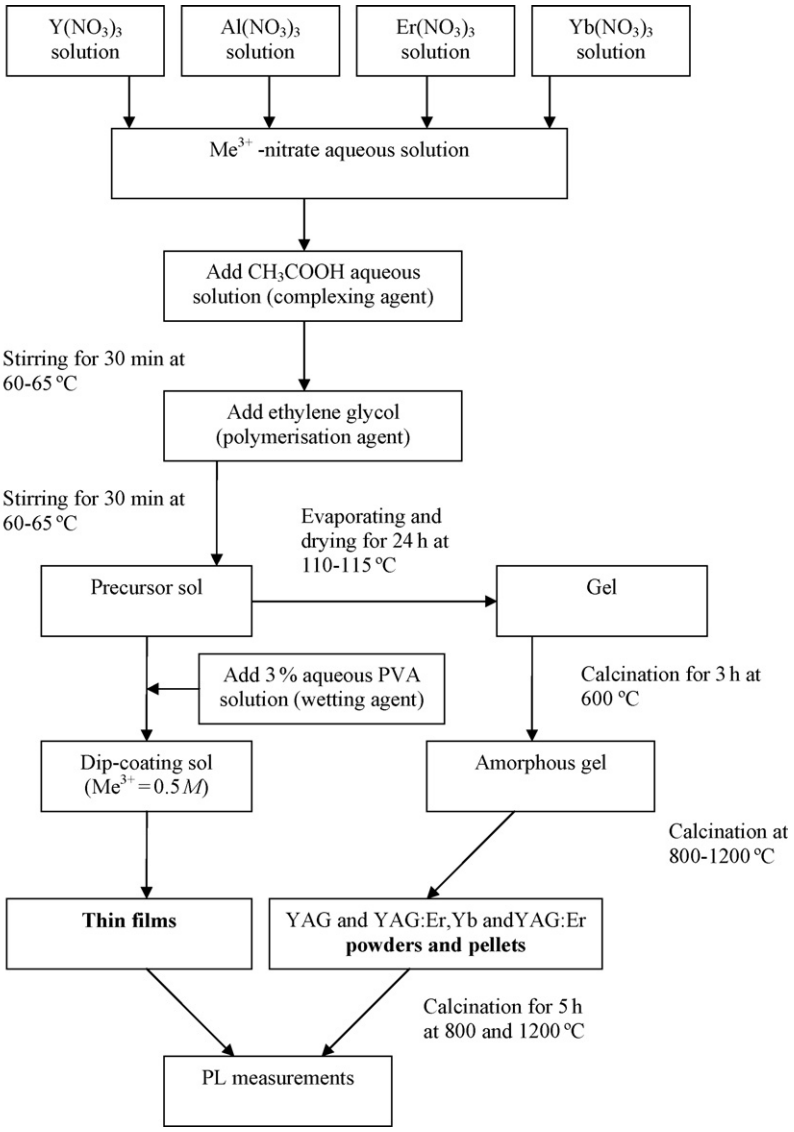

Fig. 1. Scheme of dip-coating sol, thin films, powder synthesis.

two-photon absorbing sensitized lanthanide complexes[30] and porphyrin photo-chemistry.[31,32] It was recently shown that high-performance multi-functional hybrid organic–inorganic hybrid materials can be obtained by a sol–gel procedure; here an organometallic platinum complex with strong triplet excited state absorption was introduced into a laser hardened bulk matrix with high temperature performance.[33]

Aqueous based sol–gel methods have the additional advantage that the environmental and health risks are considerably lower compared to methods based on organic solvents. However, clusters at high doping concentrations or water and similar molecules with vibration overtones in the NIR are known to quench luminescence and shorten excited state life-times of lanthanides emitting in this wavelength region, such as Er^{3+} ion.[34] Here we report the preparation of YAG and Er/Yb co-doped YAG powders and thin films by aqueous chemical solution deposition using yttrium and aluminium nitrates as precursors, acetic acid as complexing agent and ethylene glycol as polymerization agent. Moreover, the luminescent properties of Er/Yb:YAG thin films and bulk samples are also reported and the relationship between Er/Yb doping concentration and PL emission intensity is discussed. It is also demonstrated that the long excited life-times obtained in these systems can be used to harvest light at 980 nm via sequential multiphoton absorption processes.

2. Experimental

2.1. Synthesis of the sols, gels and powders

A scheme for the synthesis route of the YAG and Er/Yb:YAG sols, gels, powders and thin films is presented in Fig. 1. Yttrium nitrate hexahydrate ($Y(NO_3)_3{\cdot}6H_2O$, 99.9%, Aldrich), aluminium nitrate nonahydrate ($Al(NO_3)_3{\cdot}9H_2O$, 98.5%, Riedel-de Haen), erbium nitrate pentahydrate ($Er(NO_3)_3{\cdot}5H_2O$, 99.9%, Aldrich) and ytterbium nitrate pentahydrate ($Yb(NO_3)_3{\cdot}5H_2O$, 99.999%, Aldrich) were used as cation precursors. $Y(NO_3)_3{\cdot}6H_2O$ (7.66 g, 0.02 mol) was first dissolved in 20 mL of CO_2-free deionised water

and a stochiometric amount of $Al(NO_3)_3{\cdot}9H_2O$ (12.492 g, 0.03 mol) dissolved in 20 mL of CO_2-free deionised water was added. The acetic acid (CH_3COOH, glacial, Acros Organics; 60 mL of 0.2 M) was added as complexing agent to the yttrium–aluminium aqueous solution and the mixture was stirred for 30 min at 60–65 °C. In the following step, 2 mL of ethylene glycol (EG, ≥99%, Aldrich) was supplied to the mixture as polymerisation agent (Y^{3+} to EG molar ratio was 1:1.75) and the final solution was further stirred for 30 min to get a clear homogeneous precursor sol.

A part of the Y–Al precursor sols was evaporated at 65 °C to form transparent gels, which were further dried at 110–115 °C for 24 h and calcined at 600 °C (heating rate 30 °C/h) for 3 h and further annealed at 700, 750, 800, 850 and 900 °C (heating rate 30 °C/h) for 5 h in air with intermediate grinding between each annealing temperature.

Powders with the compositions $Y_{2.94}Er_{0.03}Yb_{0.03}Al_5O_{12}$, $Y_{2.97}Er_{0.02}Yb_{0.01}Al_5O_{12}$, $Y_{2.97}Er_{0.015}Yb_{0.015}Al_5O_{12}$, $Y_{2.97}Er_{0.01}Yb_{0.02}Al_5O_{12}$, $Y_{2.85}Er_{0.15}Al_5O_{12}$, $Y_{2.7}Er_{0.3}Al_5O_{12}$ and $Y_{2.4}Er_{0.6}Al_5O_{12}$ were prepared by an optimised route using a molar ratio of Me^{3+} (Y^{3+}, Al^{3+}, Er^{3+} and Yb^{3+}) to acetic acid and to EG corresponding to 1:1.2 and 1:5, respectively. The samples are labelled $Y_3Al_5O_{12}$:Er,Yb (1:1) (2%), $Y_3Al_5O_{12}$:Er,Yb (2:1) (1%), $Y_3Al_5O_{12}$:Er,Yb (1:1) (1%), $Y_3Al_5O_{12}$:Er,Yb (1:2) (1%), $Y_3Al_5O_{12}$:Er (5%), $Y_3Al_5O_{12}$:Er (10%) and $Y_3Al_5O_{12}$:Er (20%) in the following. The gels were calcined at 600 °C (heating rate 60 °C/h) for 3 h. Isostatically compressed pellets of the calcined powder were fired at 800 and 1200 °C (heating rate 200 °C/h) for 5 h.

2.2. Thin films processing by dip-coating

The sols described in the previous paragraph were used to produce thin films by dip-coating. An aqueous solution of 3% polyvinyl alcohol (PVA, molecular weight = 72,000, Merck–Schuchardt) was added to the precursor sol as wetting agent in order to improve the wettability of the substrate. The volume ratio of the precursor sol and PVA solution was 1:1. Y/Al and Y/Al/Er/Yb ion concentration in the aqueous dip-coating sol was 0.25 M.

Pure and Er/Yb-doped thin films of YAG were deposited on as received Si substrates (1 1 1), p-type (Crystal GmbH, Germany) using dip-coating technique (DC Mono, Nima Technology, Coventry, UK) with an immersion and withdrawal rate of 5 mm/min. For pure YAG films, five layers were deposited by a single-dipping process. In a single dipping process the deposited layer is calcined before a second layer is deposited by a new dip-coating step. For the Er–Yb doped YAG film 30 layers were deposited also by single-dipping method. Before annealing, all the deposited films were dried at room temperature for 2–3 h, then calcined at 300 and at 350 °C for 1 h, respectively with heating rate of 30 °C/h. After final deposition, the films were annealed at 600 °C for 1 h, at 800 °C for 3 h and at 900 °C for 3 h using 30 °C/h heating rate. The deposited films were calcined at 600 °C for 15 min with heating rate 300 °C/h. After final deposition the films were annealed at 900 °C for 1 h using 600 °C/h heating rate.

2.3. Morphology and structure characterization

Thermogravimetrical analysis of the precursor gel was performed with a Netzsch STA 449C *Jupiter* in air using a heating rate of 10 °C/min up to 800 °C. X-ray diffraction (XRD) analysis was performed on a Bruker AXE D8 Focus diffractometer with a LynxEye detector using Cu$K\alpha$ radiation. Average crystallite size of the films was estimated by the Scherrer equation, $d_{XRD} = K\lambda/\beta\cos\theta$, using the full-width at half maximum (FWHM) of the (4 2 0), (4 2 2), (4 3 1), (5 2 1), (5 3 2), (4 4 4), (6 4 0), and (6 4 2) reflections and for the powder samples of the (2 1 1), (4 0 0), (4 2 0), (4 2 2), (5 2 1), (5 3 2), (4 4 4), (6 4 0) and (6 4 2) reflections. The FWHM was corrected for instrumental broadening. The FWHM data did not give evidence for anisotropic crystallite shapes or crystallographic strain. Morphology and thickness of the films were observed using FE-SEM Zeiss Ultra 55 field emission scanning electron microscope with In-Lens detector.

The density of the Er and Yb doped $Y_3Al_5O_{12}$ pellets annealed at 1200 °C was measured by Archimedes method using 2-propanol. Morphology and grain size of the fracture surface of pellets were studied by low vacuum scanning electron microscope (LVSEM) (Hitachi S-3400N, Hitachi, Japan).

2.4. Luminescence measurements

Time-resolved fluorescence decays were recorded using an IBH 5000 U fluorescence lifetime spectrometer system with 1 nm resolved excitation and emission monochromators (5000 M). The IBH 5000XeF sub-microsecond xenon flash-lamp was used for multi-channel scaling (MCS) measurements. The system was equipped with a TBX-04 picosecond photon detection module for detection in the UV/visible and a Hamamatsu NIR PMT module (H9170-5) for detection in the range 900–1700 nm. Melles Griot coloured glass filters were used to block scattered light from the excitation source as well as blocking unwanted light from the laser source. The luminescence decay times were measured and analyzed using multi-channel scaling (MCS) along with the IBH Data Station v 2.1 software for operation of the spectrometer and analysis of the decay traces including reconvolution-fits. Excitation and emission spectra were obtained by locking the emission and excitation wavelengths, respectively, monitoring the detector response while scanning the appropriate monochromator.

For measuring the luminescence upon sequential multiphoton absorption, the films were excited with a 980 nm cw diode laser (Thorlabs), focused on the film surface. Luminescence spectra were collected by a lens coupled to an optical fiber and analyzed by a Hamamatsu Photonic Multichannel Analyzer (type C7473).

3. Results

3.1. Crystallisation and phase purity of bulk powders

The calcination temperature of the YAG was evaluated from TG analysis of the Y–Al–O gel powders. The TG curve pre-

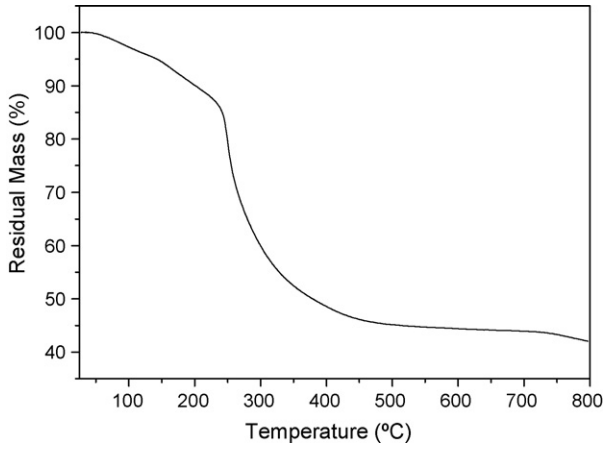

Fig. 2. Thermogravimetrical analysis of the decomposition of the Y–Al–O precursor gel.

sented in Fig. 2 demonstrates that the decomposition of the organic part of the gel occurred around 300 °C, while a minor weigh loss is observed until 800 °C. XRD of Y–Al–O gel powders annealed at different temperatures (Fig. 3) confirmed that the gel was amorphous (not shown) and that the gel decomposes to an amorphous oxide at around 300 °C. The amorphous oxide powder starts to crystallize at 700 °C and at 850 °C it is completely crystallized with crystallite size of about 70 ± 5 nm (XRD). Further annealing at higher temperature resulted in crystallite growth.

XRD of Er/Yb:YAG powders confirmed that all compositions after heat treatment at 1200 °C (Fig. 4) were phase pure and no impurity phases such as $YAlO_3$ (YAP), $Y_4Al_2O_9$ (YAM), Er_2O_3 or Yb_2O_3 were observed. The average crystallite size of the powders sintered at 1200 °C was calculated to be 88 ± 5 nm and the density of pellets annealed at 1200 °C was 50% of theoretical. The cross-section SEM analysis of pellets heat treated at 1200 °C confirmed that porous nano-crystalline samples were obtained.

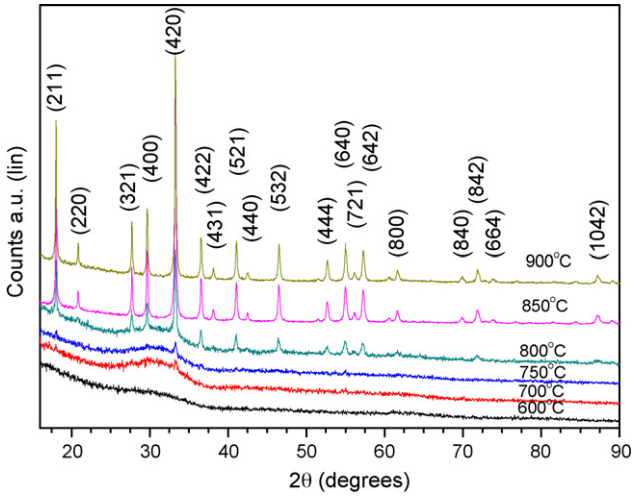

Fig. 3. X-ray diffraction patterns of YAG powders derived from precursor Y–Al–O gel annealed at 600–900 °C.

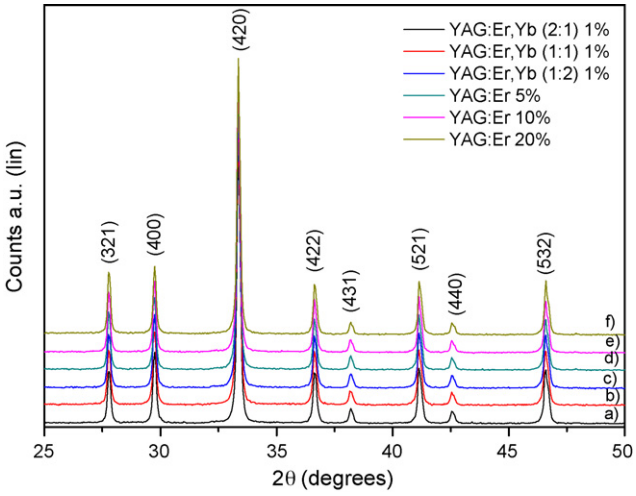

Fig. 4. X-ray diffraction patterns of $Y_3Al_5O_{12}$:Er,Yb (2:1) (1%), $Y_3Al_5O_{12}$:Er,Yb (1:1) (1%), $Y_3Al_5O_{12}$:Er,Yb (1:2) (1%), $Y_3Al_5O_{12}$:Er (5%), $Y_3Al_5O_{12}$:Er (10%) and $Y_3Al_5O_{12}$:Er (20%) powder samples annealed at 1200 °C.

3.2. Thin films

The surface morphology and cross-section FE-SEM images of the deposited YAG films are shown in Fig. 5. The deposited films appear smooth and homogeneous and consist of densely packed nano-crystalline grain after annealing at 900 °C (Fig. 5(d)). The thickness of the deposited films was determined to be in the range of 200–250 nm showing that thickness per single dipped layer was 40–50 nm. Cross-section image of the $Y_3Al_5O_{12}$:Er,Yb (1:1) (2%) film deposited from the modified sol (Fig. 5(e)) demonstrates a homogeneous film of densely packed nano-crystalline particles. The thickness of the deposited film is 1 μm confirming that the thickness per single dipped layer was 40 nm.

The Bragg reflections in the XRD pattern of the deposited YAG film annealed at 900 °C were assigned to the polycrystalline YAG phase which is consistent with literature (JCPDS No. 33–40) (data not presented). No other intermediate phases such as YAP and YAM were observed. The average crystallite size of the deposited films was estimated to be 27 ± 5 nm.

3.3. Photoluminescence properties

The samples of $Y_3Al_5O_{12}$:Er,Yb (1:2) (1%), $Y_3Al_5O_{12}$:Er (5%), $Y_3Al_5O_{12}$:Er (10%) and $Y_3Al_5O_{12}$:Er (20%) showed characteristic Er^{3+} luminescence between 1350 and 1600 nm for excitation in the UV and visible region as shown in Fig. 6. The main emission peak occurs at ~1530 nm and is attributed to the intra-4f $^4I_{13/2} \rightarrow {}^4I_{15/2}$ transition of the Er^{3+} ion. Representative excitation spectra obtained by scanning the excitation monochromator while monitoring the Er^{3+} luminescence at 1530 nm are presented in Fig. 7. The main excitation peaks are observed at 455 and 255 nm, with weaker features observed at 525 and 660 nm. The absorption channels correspond to direct excitation of the transitions $^4I_{15/2} \rightarrow {}^4F_{5/2}$ (455 nm emission),

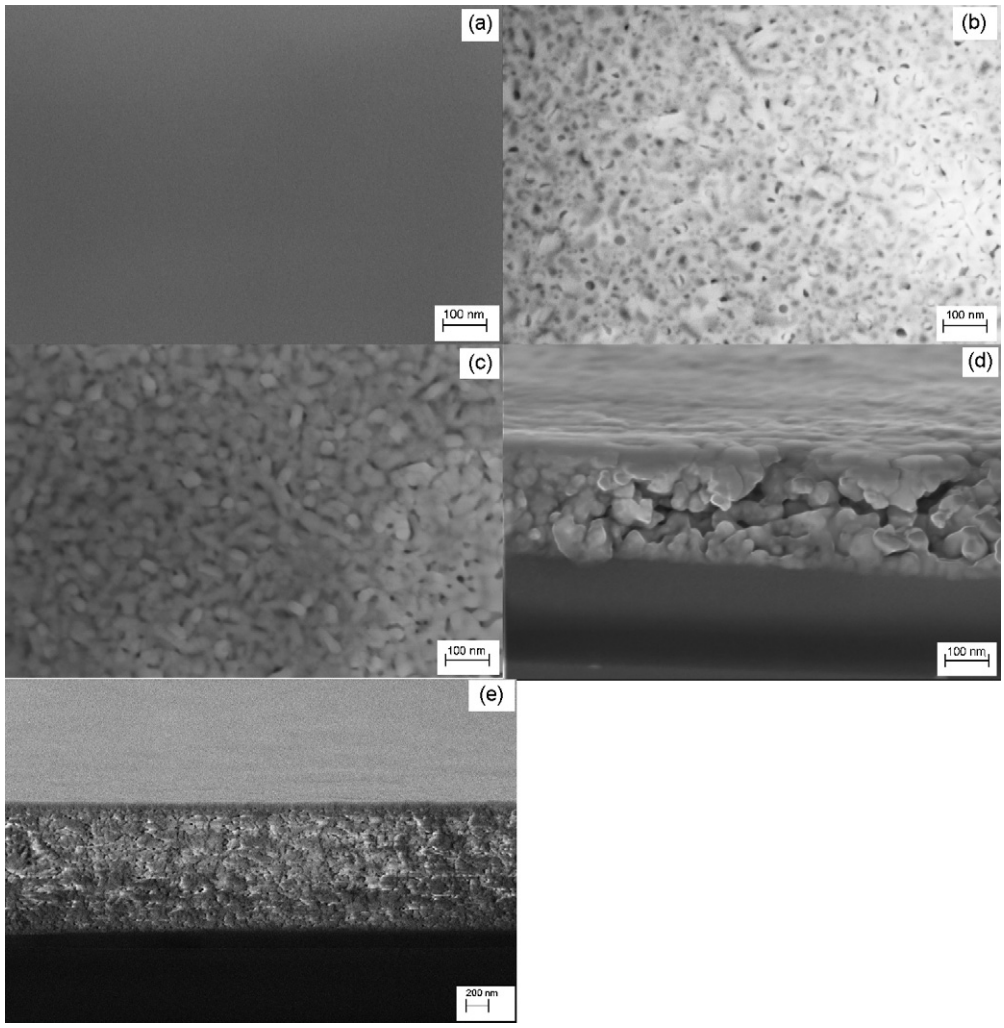

Fig. 5. Surface and cross-sectional FE-SEM images of YAG (one layer film annealed at 350 °C (a); five layer films annealed at 600 °C (b) and five layer films annealed at 900 °C (c) and (d)) and $Y_3Al_5O_{12}$:Er,Yb (1:1) 2 mol% doping (30-layer film annealed at 900 °C (e)) films derived from 0.25 M dip-coating sols.

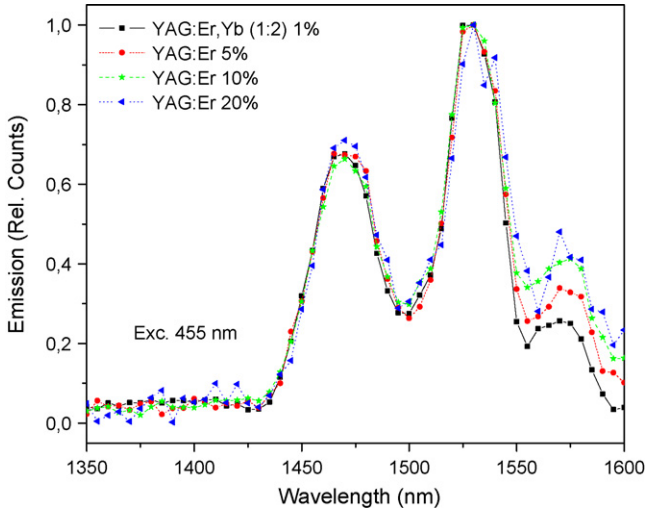

Fig. 6. Emisison spectra of $Y_3Al_5O_{12}$:Er,Yb (1:2) (1%), $Y_3Al_5O_{12}$:Er (5%), $Y_3Al_5O_{12}$:Er (10%) and $Y_3Al_5O_{12}$:Er (20%) pellets samples under 455 nm excitation.

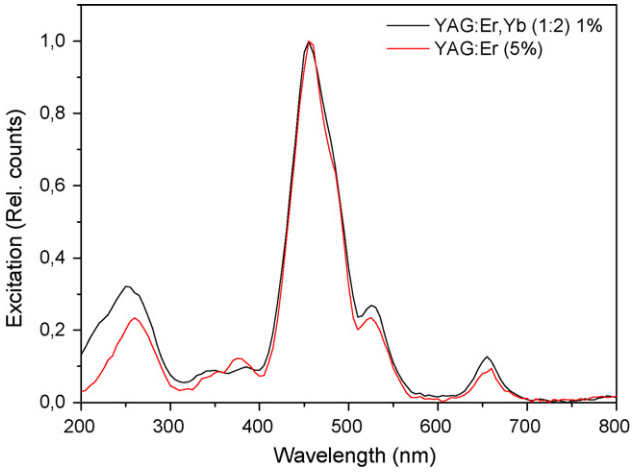

Fig. 7. Excitation spectra of $Y_3Al_5O_{12}$:Er,Yb (1:2) (1%) and $Y_3Al_5O_{12}$:Er (5%) pellets samples.

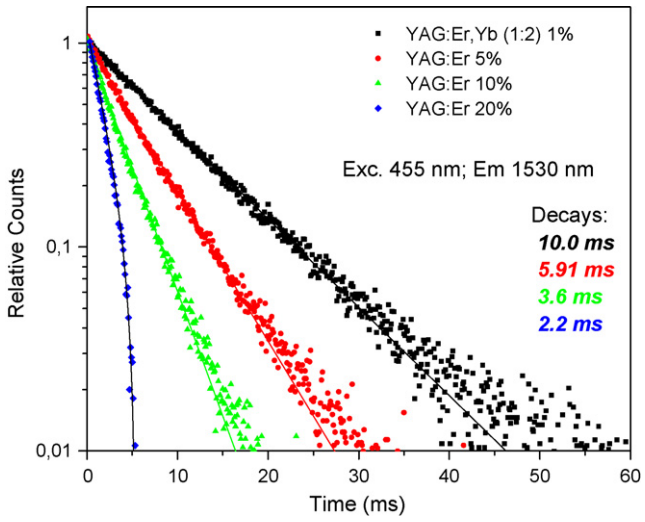

Fig. 8. Time decay curves at 1530 nm under 455 nm excitation of $Y_3Al_5O_{12}$:Er,Yb (1:2) (1%), $Y_3Al_5O_{12}$:Er (5%), $Y_3Al_5O_{12}$:Er (10%) and $Y_3Al_5O_{12}$:Er (20%) pellets samples. The continuous lines are fitting curves.

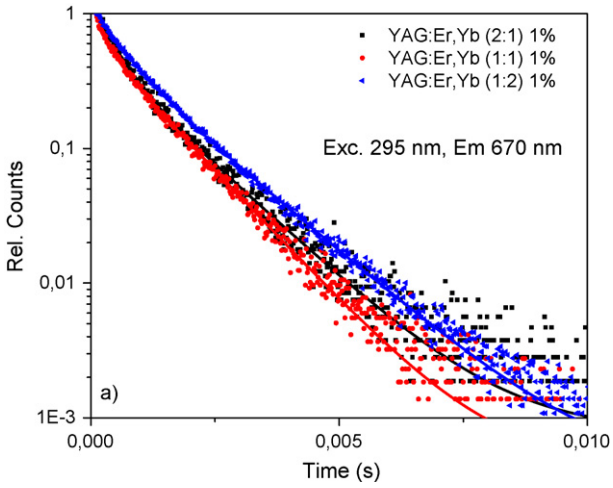

Fig. 9. Time decay curves at 670 nm under 295 nm excitation of $Y_3Al_5O_{12}$:Er,Yb (2:1) (1%), $Y_3Al_5O_{12}$:Er,Yb (1:1) (1%) and $Y_3Al_5O_{12}$:Er,Yb (1:2) (1%) pellets samples. The continuous lines are fitting curves.

$^4I_{15/2} \rightarrow {}^2D_{7/2}$ (255 nm emission), $^4I_{15/2} \rightarrow {}^2H_{11/2}$ (525 nm emission) and $^4I_{15/2} \rightarrow {}^4F_{9/2}$ (660 nm emission).

Time resolved measurements gave further information of the relaxation of the Er^{3+} levels. The decay times of the $^4I_{13/2} \rightarrow {}^4I_{15/2}$ transition for the same samples as shown in Fig. 6, for excitation at 455 nm and emission at 1530 nm, are depicted in Fig. 8. For the low Er^{3+} concentration one observes a long decay time of 10 ms, which is of similar magnitude as observed for Er^{3+} in Er,Yb:YAG.[35,36] As the concentration of Er^{3+} increases the luminescence gradually is quenched to reach a decay time of 2.2 ms for the sample with 20% of Er dopant. The faster drop of the decays for higher Er^{3+} concentrations suggest cross-relaxation process to be involved.

The samples also exhibited weak luminescence emission in the visible. Emission spectra of $Y_3Al_5O_{12}$:Er,Yb (2:1) (1%), $Y_3Al_5O_{12}$:Er,Yb (1:1) (1%), $Y_3Al_5O_{12}$:Er,Yb (1:2) (1%) pellets subjected to excitation pulses at 295 nm showed that the latter has the most intense emission in the visible region with distinct peaks at 670 and 770 nm (data not shown). The time-resolved measurements resulted in the decays as shown in Fig. 9. Compared to the emission in the IR, the emission decays at 670 and 770 nm were not mono-exponentials and two decay constants had to be assumed to fit all cases. The detailed analysis is summarized in Table 1. As can be judged from the appearance of the decay traces there are only minor differences in the decay times for the emissions in the visible as the decay times are hardly changed with dopant concentration as was observed for the $^4I_{13/2} \rightarrow {}^4I_{15/2}$ luminescence in the IR.

3.4. Up-conversion photoluminescence

It was also investigated the possibility to stimulate further sequential excitation of the Er^{3+} doped samples by monitoring the up-conversion photoluminescence by excitation at 980 nm. Emission spectra of the bulk samples are presented in Fig. 10. The observed luminescence peaks in the visible region at 520–570 and 640–680 nm are due to the radiative transitions in the Er^{3+} ions from $^2H_{11/2}$ and $^4S_{3/2}$ to $^4I_{15/2}$ (green emission), and from $^4F_{9/2}$ to $^4I_{15/2}$ (red emission), respectively. $Y_3Al_5O_{12}$:Er,Yb (2:1) (1%), $Y_3Al_5O_{12}$:Er,Yb (1:1) (1%), $Y_3Al_5O_{12}$:Er,Yb (1:2) (1%) bulk samples with low doping concentrations showed higher green emission intensity than emission intensity in the red spectra region. When the Er^{3+} concentration increases from 5, 10 to 20%, the red up-converted luminescence intensity is enhanced. In up-conversion photoluminescence emission spectrum of the $Y_3Al_5O_{12}$:Er,Yb (1:1) (2%) thin film sample the same green/red emission intensity ratio was observed (data not shown). For thin film samples with low doping concentration $^2H_{11/2}/{}^4S_{3/2} \rightarrow {}^4I_{15/2}$ was found to dominate over $^4F_{9/2} \rightarrow {}^4I_{15/2}$ transition.

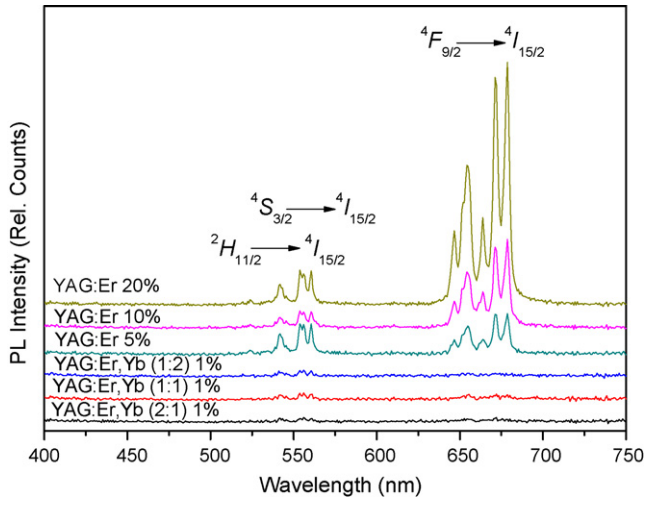

Fig. 10. PL up-conversion emission spectra of $Y_3Al_5O_{12}$:Er,Yb (2:1) (1%), $Y_3Al_5O_{12}$:Er,Yb (1:1) (1%), $Y_3Al_5O_{12}$:Er,Yb (1:2) (1%), $Y_3Al_5O_{12}$:Er (5%), $Y_3Al_5O_{12}$:Er (10%) and $Y_3Al_5O_{12}$:Er (20%) pellets samples annealed at 1200 °C after IR exitation at 980 nm (150 mW, 500 ms).

Table 1
Decay times for emision at 670 and 770 nm for $Y_3Al_5O_{12}$:Er,Yb (2:1) (1%), $Y_3Al_5O_{12}$:Er,Yb (1:1) (1%) and $Y_3Al_5O_{12}$:Er,Yb (1:2) (1%) pellets samples annealed at 1200 °C, excited at 295 nm. The value in parenthesis behind the decay constants is the relative weight for each component of the fit.

Sample	Decay ms (rel. weight %) at 670 nm	Decay ms (rel. weight %) at 770 nm
$Y_3Al_5O_{12}$:Er,Yb (2:1) (1%)	$\tau_1 = 0.388$ (24%)	$\tau_1 = 2.72$ (14%)
	$\tau_2 = 1.28$ (76%)	$\tau_2 = 10.4$ (86%)
$Y_3Al_5O_{12}$:Er,Yb (1:1) (1%)	$\tau_1 = 0.389$ (13%)	$\tau_1 = 3.20$ (17%)
	$\tau_2 = 1.11$ (86%)	$\tau_2 = 10.1$ (83%)
$Y_3Al_5O_{12}$:Er,Yb (1:2) (1%)	$\tau_1 = 0.507$ (23%)	$\tau_1 = 3.54$ (19%)
	$\tau_2 = 1.39$ (77%)	$\tau_2 = 11.5$ (81%)

4. Discussion

The aqueous chemical solution deposition route was demonstrated to produce single phase YAG powders. The sol–gel route was also demonstrated to yield homogeneous, smooth and nano-crystalline YAG films on silicon substrates by dip-coating. According to the surface morphology (Fig. 5(a–d)), the films appear crack-free, smooth and homogeneous. The thin films were also shown to consist of densely packed nano-crystalline grains in the range 27 ± 5 nm. To simplify the preparation route, multi-dipping deposition (five immersions before each calcination) was also performed. The films produced by the multi-dipping procedure and calcined at 900 °C exhibited very similar morphology as films deposited by the single dipping method.

The films completely covered the substrate which indicates good wettability of the solution on the substrates and significant adhesion strength between the substrate and the deposited layer. Other concentrations of PVA solutions (1, 2, 5 and 10%) as wetting agent were also tested in the dip-coating procedure. The higher concentrations of the PVA solution led to the formation of a thick, inhomogeneous layer of deposited Y–Al–O gel. On the other hand, the low concentrations of PVA led to an undesirable decrease in the wettability of the substrate, hence a 3% solution was regarded as the optimum.

In the films annealed at 600 °C, homogeneous distribution of fine pores was observed (Fig. 5(b)). With increasing annealing temperature up to 900 °C, the porosity decreased leading to film densification. It should be noted that density gradients along the film surface was observed. Hence, further optimization of e.g., annealing temperature is necessary to remove all porosity. It was however shown, that with careful control of sol composition and dip-coating conditions it is possible to produce nano-crystalline YAG thin films without the presence of other intermediate phases by this simple aqueous route.

The optical properties of the (Er, Yb) doped YAG prepared by the present sol–gel synthesis were similar to the properties reported for similar materials prepared by another preparation routes.[14,23] In the following the optical properties are discussed in detail.

The position of the luminescence bands in the spectrum is characteristic for a specific lanthanide ion. The Er^{3+} is a widely used system in fiber optics and photonics due to its emission at 1.5 μm, but it also emit in the visible region. Er^{3+} ion has incomplete 4f electronic shell which is shielded by closed 5s and 5p shells resulting in rather sharp luminescence bands.[37,38] In particular, a quantum efficiency of the $^4I_{13/2} \rightarrow {}^4I_{15/2}$ transition in the Er^{3+} ion is very high.[39] However, for low Er^{3+} ion concentrations the absorption coefficients are very small. In order to increase luminescence generally Yb^{3+} is used as co-dopant for Er^{3+} systems which has a very simple f–f energy level structure. Besides the $^2F_{7/2}$ ground multiplet, there is only the $^2F_{5/2}$ excited multiplet at around 1 μm in Yb^{3+} ion. Also, the energy of $^2F_{5/2}$–Yb^{3+} state is very similar to $^4I_{11/2}$–Er^{3+} state. For these reasons, the energy is mostly absorbed by Yb^{3+} ion and transferred to Er^{3+} ion ($^2F_{5/2}(Yb^{3+}) \rightarrow {}^4I_{11/2}(Er^{3+})$) by dipole-dipole interaction.[35]

Because of possible energy level transitions both Er^{3+} and Yb^{3+} ions are used extensively in up-conversion (anti-Stokes emission) process. In Er–Yb up-conversion process, two mechanisms ESA (excited state absorption) and ETU (energy transfer up-conversion) are involved. ESA is operative via the channel $^4I_{15/2} \rightarrow {}^4I_{11/2} \rightarrow {}^4F_{7/2}$ and ETU from $^2F_{5/2} \rightarrow {}^2F_{7/2}$:$^4I_{11/2} \rightarrow {}^4F_{7/2}$ (of neighbouring Yb^{3+}) and from $^4I_{11/2} \rightarrow {}^4I_{15/2}$:$^4I_{11/2} \rightarrow {}^4F_{7/2}$ (of neighbouring Er^{3+}), followed by photon relaxation to the $^2H_{11/2}$ or $^4S_{3/2}$ for green emission and to the $^4F_{9/2}$ for the red emission.[39–42] The up-conversion luminescence is very weak in the samples with 1 mol% Er/Yb doping concentrations. At low doping concentrations the predominant mechanism is excited state absorption (ESA). In this process Er^{3+} by absorbing the IR photon (ground state absorption, GSA) is excited to the $^4I_{9/2}$ level from where it relaxes nonradiative to the $^4I_{11/2}$ level. By subsequent absorption of second IR photon, the $^4I_{11/2} \rightarrow {}^4F_{3/2}$ transition occurs (ESA). From the metastable $^4F_{3/2}$ level, the nonradiative multiphoton relaxation (NR) can occur to the $^4S_{3/2}$ and $^4F_{9/2}$ levels, which are more stable than $^2F_{5/2}$, $^4F_{7/2}$ or $^2H_{11/2}$ levels.

However, the absolute intensities in the bulk materials increase with increasing Er^{3+} doping concentration from 5 to 20 mol%. At high doping concentrations the cooperative energy transfer (CET) process ($^4F_{7/2}$, $^4I_{11/2} \rightarrow 2{}^4F_{9/2}$ and $^4S_{3/2}$, $^4I_{1/2} \rightarrow 2{}^4F_{9/2}$) operate between two nearby Er^{3+} ions. Consequently, the $^2H_{11/2} \rightarrow {}^4I_{15/2}$ has very weak intensity and the emission from $^4F_{9/2}$ to $^4I_{15/2}$ becomes more dominant in comparison with $^2H_{11/2}$, $^4S_{3/2}$ to $^4I_{15/2}$ transitions.

5. Conclusion

The present report demonstrate a successful aqueous sol–gel route to YAG powders and thin film using nitrate cation pre-

cursors, acetic acid as complexing agent and ethylene glycol as polymerization agent. The gels were shown to decompose to an amorphous oxide and the crystallisation of the amorphous gel was characterized. Fabrication of homogeneous, crack-free pure YAG and Er/Yb-doped YAG thin films by dip-coating of the aqueous sol deposited on Si (1 1 1) substrates were demonstrated. The photoluminescence up-conversion (anti-Stokes emission) properties of the Er,Yb:YAG materials are reported. The photoluminescence as well as up-conversion (anti-Stokes emission) processes demonstrated significant influence of the dopant level.

References

1. Hirata GA, Mckittarick J, Devlin D. Growth and analysis of red, green and blue luminescent oxide thin films. *Surf Rev Lett* 1998;**5**(1):413–7.
2. Potdevin A, Chadeyron G, Boyer D, Mahiou R. Optical properties upon vacuum ultraviolet excitation of sol–gel based $Y_3Al_5O_{12}$:Tb^{3+}, Ce^{3+} powders. *J Appl Phys* 2007;**102**(7):073536–73546.
3. Zorenko Yu, Gorbenco V, Konstankevych I, Voloshinovskii A, Stryganyuk G, Mikhailin V, Kolobanov V, Spassky D. Single-crystalline films of Ce-doped YAG and LuAG phosphors: advantages over bulk crystals analogues. *J Lumin* 2005;**114**(2):85–94.
4. Uhlich D, Huppertz P, Wiechert DU, Jüstel T. Preparation and characterization of nanoscale lutetium aluminium garnet (LuAG) powders doped by Eu^{3+}. *Opt Mater* 2007;**29**(11):1505–9.
5. Rabinovitch Y, Bogicevic C, Karolak F, Tetard D, Dammak H. Freeze-dried nanometric neodymium-doped YAG powders for transparent ceramics. *J Mater Process Technol* 2008;**199**(1–3):314–20.
6. Pullar RC, Taylor MD, Bhattacharya AK. The sintering behaviour, mechanical properties and creep resistance of aligned polycrystalline yttrium aluminium garnet (YAG) fibres produced from an aqueous sol–gel precursor. *J Eur Ceram Soc* 1999;**19**(9):1747–58.
7. Karato S, Wang Z, Fujino K. High-temperature creep of yttrium–aluminum garnet single crystals. *J Mater Sci* 1994;**29**(24):6458–62.
8. Bonner WA. Epitaxial growth of garnets for thin film lasers. *J Electron Mater* 1974;**3**(1):193–208.
9. Van der Weg WG, van Tol MW. Saturation effect of cathodoluminescence in rare-earth activated epitaxial $Y_3Al_5O_{12}$ layers. *Appl Phys Lett* 1981;**38**(9):705–7.
10. Rotman SR, Tandon RP, Tuller HL. Defect–property correlations in garnet crystals: The electrical conductivity and defect structure of luminescent cerium-doped yttrium aluminium garnet. *J Appl Phys* 1985;**57**(6):1951–5.
11. Rotman SR, Tuller HL. Defect-property correlations in garnet crystals. III. The electrical conductivity and defect structure of luminescent nickel-doped yttrium aluminium garnet. *J Appl Phys* 1987;**62**(4):1305–12.
12. Schuh L, Metselaar R, de With G. Electrical transport and defect properties of Ca- and Mg-doped yttrium aluminium garnet ceramics. *J Appl Phys* 1989;**66**(6):2627–32.
13. Robertson JM, van Tol MW. Cathodoluminescent garnet layers. *Thin Solid Films* 1984;**114**(1–2):221–40.
14. Wang W-N, Widiyastuti W, Ogi T, Lenggoro IW, Okuyama K. Correlations between crystallite/particle size and photoluminescence properties of submicrometer phosphors. *Chem Mater* 2007;**19**(7):1723–30.
15. Hsu CT, Yen SK. Electrochemical synthesis of thin film YAG on inconel substrate. *Electrochem Solid-State Lett* 2006;**9**(4):D9–12.
16. Mizoguchi Y, Kagawa M, Syono Y, Hirai T. Film synthesis of $Y_3Al_5O_{12}$ and $Y_3Fe_5O_{12}$ by the spray-inductively coupled plasma technique. *J Am Ceram Soc* 2001;**84**(3):651–3.
17. Parukuttyamma SD, Margolis J, Liu H, Grey CP, Sampath S, Herman H, Parise JB. Yttrium aluminum garnet (YAG) films through a precursor plasma spraying technique. *J Am Ceram Soc* 2001;**84**(6):1906–8.
18. Diaz-Torres LA, De la Rosa E, Salas P, Angeles-Chavez C, Arenas LB, Nieto J. Nanoparticle thin films of nanocrystalline YAG by pulsed laser deposition. *Opt Mater* 2005;**27**(7):1217–20.
19. Hay RS. Phase transformations and microstructure evolution in sol–gel derived yttrium–aluminium garnet films. *J Mater Res* 1993;**8**(3):578–604.
20. Wu Y-C, Parola S, Mugnier J. Preparation and characterization of sol–gel derived YAG optical planar waveguide. Advances in optical thin films. In: Arma C, Kaiser N, Macleod HA, editors. *Proceedings of SPIE, vol. 5250*. 2003. p. 581–8.
21. Wu Y-C, Parola S, Marty O, Villanueva-Ibanez M, Mugnier J. Structural characterizations and waveguiding properties of YAG thin films obtained by different sol–gel processes. *Opt Mater* 2005;**27**(9):1471–9.
22. Bai GR, Chang HLM, Foster CM. Preparation of single-crystal $Y_3Al_5O_{12}$ thin film by metalorganic chemical vapour deposition. *Appl Phys Lett* 1994;**64**(14):1777–9.
23. Jia PY, Lin J, Han XM, Yu M. Pechini sol–gel deposition and luminescence properties of $Y_3Al_{5-x}Ga_xO_{12}$:Ln^{3+} (Ln^{3+} = Eu^{3+}, Ce^{3+}, Tb^{3+}; $0 \le x \le 5$) thin films. *Thin Solid Films* 2005;**483**(1–2):122–9.
24. Costa VC, Lochhead MJ, Bray KL. Fluorescence line-narrowing study of Eu^{3+}-doped sol–gel silica: effect of modifying cations on the clustering of Eu^{3+}. *Chem Mater* 1996;**8**(3):783–90.
25. Weber MJ. Science and technology of laser glass. *Non-Cryst Solids* 1990;**123**(1–3):208–22.
26. Glomm WR, Volden S, Sjöblom J, Lindgren M. Photophysical properties of ruthenium(II) tris(2,2′-bipyridine) and europium(III) hexahydrate salts assembled into sol–gel materials. *Chem Mater* 2005;**17**(22):5512–20.
27. Kawa M, Frechet JMJ. Self-assembled lanthanide-cored dendrimer complexes: enhancement of the luminescence properties of lanthanide ions through site-isolation and antenna effects. *Chem Mater* 1998;**10**(1):286–96.
28. Vestberg R, Westlund R, Eriksson A, Lopes C, Carlsson M, Eliasson B, Glimsdal E, Lindgren M, Malmström E. Dendron decorated platinum(II) acetylides from optical power limiting. *Macromolecules* 2006;**39**(6):2238–46.
29. Lindgren M, Minaev B, Glimsdal E, Vestberg R, Westlund R, Malmström E. Electronic states and phosphorescence of dendron functionalized platinum (II) acetylides. *J Lumin* 2007;**124**(2):302–10.
30. Bouit P-A, Kamada K, Feneyrou P, Berginc G, Toupet L, Maury O, Andraud C. Two-photon absorption-related properties of functionalized BODIPY dyes in the infrared range up to telecommunication wavelengths. *Adv Mater* 2009;**21**(10–11):1151–4.
31. Dichtel WR, Hecht S, Fréchet JMJ. Functionally layered dendrimers: A new building block and its application to the synthesis of multichromophoric light-harvesting systems. *Org Lett* 2005;**7**(20):4451–4.
32. Vestberg R, Nystrom A, Lindgren M, Malmstrom E, Hult A. Porphyrin-cored 2,2-bis(methylol)propionic acid dendrimers. *Chem Mater* 2004;**16**(14):2794–804.
33. Zieba R, Desroches C, Chaput F, Carlsson M, Eliasson B, Lopes C, Lindgren M, Parola S. Preparation of functional hybrid glass material from platinum (II) complexes for broadband nonlineat absorption of light. *Adv Funct Mater* 2009;**19**(2):235–41.
34. Parker D. Luminescent lanthanide sensors for pH, pO_2 and selected anions. *Coord Chem Rev* 2000;**205**:109–30.
35. Schweizer T, Jensen T, Heumann E, Huber G. Spectroscopic properties and diode pumped 1.6 μm laser performance in Yb-codoped Er:$Y_3Al_5O_{12}$ and Er:Y_2SiO_5. *Opt Commun* 1995;**118**(5–6):557–61.
36. Denker B, Galagan B, Osiko V, Sverchkov S, Balbashov AM, Hellström JE, Pasiskevicius V, Laurell F. Yb^{3+}, Er^{3+}:YAG at high temperatures: Energy transfer and spectroscopic properties. *Opt Commun* 2007;**271**(1):142–7.
37. Nishi M, Tanabe S, Inoue M, Takahashi M, Fujita K, Hirao K. Optical-telecommunication-band fluorescence properties of Er^{3+}-doped nanocrystals synthesized by glycothermal method. *Opt Mater* 2005;**27**(4):655–62.
38. Polman A. Erbium implanted thin film photonic materials. *Appl Phys Lett* 1997;**82**(1):1–39.
39. Auzel F. Upconversion in anti-Stokes processes with f and d ions in solids. *Chem Rev* 2004;**104**(1):139–74.
40. Kenyon AJ. Recent developments in rare-earth doped materials for optoelectronics. *Prog Quantum Electron* 2002;**26**(4–5):225–84.

41. Strümpel C, McCann M, Beaucarne G, Arkhipov V, Slaoui A, Švrček V, del Canizo C, Tobias I. Modifying the solar spectrum to enhance silicon solar cell efficiency—an overview of available materials. *Sol Energy Mater Sol Cells* 2007;**91**(4):238–49.

42. Qin G, Lu J, Bisson JF, Feng Y, Ueda K, Yagi H, Yanagitani T. Upconversion luminescence of Er^{3+} in highly transparent YAG ceramics. *Solid State Commun* 2004;**132**(2):103–6.